BNL-76856-2006-BC

Chemistry of SO_2 and $DeSO_x$ Processes on Oxide Nanoparticles

José A. Rodriguez

To be published in "Synthesis, Properties and Applications of Oxide Nanomaterials"

June 2006

Chemistry Department

Brookhaven National Laboratory
P.O. Box 5000
Upton, NY 11973-5000
www.bnl.gov

DISCLAIMER

Chapter 20

Chemistry of SO_2 and $DeSO_x$ Processes on Oxide Nanoparticles

José A. Rodriguez
Department of Chemistry
Brookhaven National Laboratory
Upton, NY 11973, USA
* E-mail: Rodrigez@bnl.gov, FAX: 1-631-344-2246

Table of Contents

20.1 Introduction

20.2 Chemistry of SO_2 on bulk oxides

20.3 Chemistry of SO_2 and DeSOx process on oxide nanoparticles
- 20.3.1 Interaction with CaO, MgO and SrO
- 20.3.2 Interaction with Al_2O_3 and Al_2O_3/MgO
- 20.3.3 Interaction with Fe_2O_3, Fe_2O_3/CaO and Fe_2O_3/SrO
- 20.3.4 Interaction with CeO_2 and doped-ceria

20.4 Conclusions

1. Introduction

The chemistry of sulfur dioxide (SO_2) on oxide nanoparticles is receiving a lot of attention due to its importance in the industrial production of sulfuric acid (1) and environmental catalysis (2,3,4). Sulfur-containing molecules are common impurities present in coal and crude oil. SO_2 is one of the major air pollutants released to the atmosphere as a result of the combustion of fuels in power plants, factories, houses and transportation (2). It contributes to the generation of smog and constitutes a serious health hazard for the respiratory system (2). After its oxidation and reaction with water in the atmosphere, it is responsible for the acid rain that kills vegetation and corrodes buildings and monuments in modern cities (2). In addition, the SO_2 produced by the combustion of sulfur-containing fuels in automotive engines poisons the catalysts that are used for the removal of CO and NO in exhaust catalytic converters ($2CO + O_2 \rightarrow 2CO_2$; $2CO + 2NO \rightarrow 2CO_2 + N_2$) (4,5). When SO_2 is present in the catalytic converter at high concentrations, it dissociates on the precious-metal component of the catalyst (Rh, Pd or Pd), blocking active sites and reducing also the overall activity of the system through medium or long-range electronic effects (6,7). At the levels of 5 to 20 ppm currently present in the typical automotive exhaust, SO_2 interacts primarily with the ceria component of the catalytic converter, and the poisoning of this oxide is a major concern nowadays (8,9,10).

Governments are constantly tightening regulations to limit the production of SO_2 and emission of sulfur compounds into the air (3-5). Over the past 30 years several processes have been proposed and developed for the removal of SO_2 from exhaust systems, DeSOx operations, (3-5,11). There is still not universally acceptable solution to this problem. Due to their low cost, oxides are frequently used as sorbents or scrubbers for trapping the SO_2 molecule in industrial

processes (11). Also, there is a general interest (3,4,11-15) in using oxides as catalysts for the Claus reaction ($SO_2 + 2H_2S \rightarrow 2H_2O + 3S_n$) and the reduction of sulfur dioxide by CO ($SO_2 + 2CO \rightarrow 2CO_2 + S_n$). In these reactions, the rupture of the S-O bonds on the oxide catalyst is one of the most difficult steps.

This chapter presents an overview of recent studies that focus on the chemistry of SO_2 and DeSOx processes on oxide nanoparticles. In principle, the unique electronic and structural properties of oxide nanostructures can lead to a high activity for the cleavage of S-O bonds. A comparison to studies performed using single crystals like ZnO(0001), MgO(100) or CeO_2(110) allows a detailed analysis of structure sensitivity and the impact of defects and O vacancies. This chapter is organized as follows. First, a brief general description of the behavior of SO_2 on bulk oxide systems is presented. This is followed by a more detailed description of the interaction of SO_2 with nanoparticles of CaO, MgO, SrO, Al_2O_3, Al_2O_3/MgO, Fe_2O_3, Fe_2O_3/CaO, CeO_2, $Ce_{1-x}Zr_xO_2$ and $Ce_{1-x}Ca_xO_{2-y}$. Approaches useful for facilitating or promoting the dissociation of SO_2 on oxide nanoparticles are discussed.

2. Chemistry of SO_2 on bulk oxides

A study of the interaction of SO_2 with CeO_2 is interesting for two basic reasons. First, ceria doped with copper or other metals is able to catalyze the reduction of SO_2 by CO (14,15). And second, the SO_2 formed during the combustion of fuels in automotive engines can affect the performance of the CeO_2 or $Ce_{1-x}Zr_xO_2$ present in catalysts used for reducing CO and NOx emissions (8,9,10). The species responsible for ceria deactivation is mainly attributed to cerium sulfate, which blocks the Ce^{3+} sites for the redox cycle in the process of oxygen storage/release

(8,9,10). Reaction of SO_2 with CeO_2 powders and polycrystalline ceria films supported on Pt(111) at 25 ^oC shows sulfate (SO_4) as the main surface species as evidenced by a combination of XANES, temperature programmed desorption (TPD), and high-resolution photoemission (16). Photoemission studies for the adsorption of SO_2 on $CeO_2(111)$ and $Ce_{1-x}Zr_xO_2(111)$ point to the formation of a SO_x species on the surface that could be either SO_3 or SO_4 (17,18). The identification of this species on the basis of only photoemission is not conclusive (17). To address this issue, X-ray absorption near-edge spectroscopy (XANES) was used to study the interaction of SO_2 with $CeO_2(111)$ and $Ce_{1-x}Zr_xO_2(111)$ surfaces (19). Figure 1 shows S K-edge spectra for the adsorption of SO_2 on $CeO_2(111)$ and $Ce_{0.7}Zr_{0.3}O_2(111)$ surfaces at room temperature. A comparison to the corresponding peak positions for sulfates and sulfites (19). indicates that SO_4 is the main species formed on the oxide surfaces with a minor concentration of SO_3. There is no dissociation of the adsorbate.

The top layer of $CeO_2(111)$ and $Ce_{0.7}Zr_{0.3}O_2(111)$ contains only O atoms, see Figure 2. The adsorption of SO_2 on these O atoms would yield directly sulfite or sulfate species:

$$SO_{2,gas} + O_{lattice} \rightarrow SO_{3,ads} \qquad (1)$$

$$SO_{3,ads} + O_{lattice} \rightarrow SO_{4,ads} \qquad (2)$$

There are "holes" in the top layer of $CeO_2(111)$ and $Ce_{0.7}Zr_{0.3}O_2(111)$ that expose Ce and Zr cations in the second layer, see Figure 2. These cations have all their O neighbors (eight in total) and interact very weakly with an adsorbed SO_2 molecule (17).

Figure 3 displays photoemission data for the adsorption of SO_2 at 300 K on a MgO(100) crystal, bottom panel, and a MgO(100) epitaxial film grown on a Mo(100) substrate, top panel (20). The (100) face of MgO consist of a 50%-50% mixture of Mg and O atoms. The

photoemission data indicate that only the O atoms interact strongly with SO_2 forming a mixture of SO_3 and SO_4 species on the oxide surface (20). An identical result was observed with XANES after exposing MgO powders to moderate pressures of SO_2 (21). The metal centers of MgO interact weakly with SO_2 and are not able to dissociate the molecule (20,21). In general, bulk powders of pure stoichiometric oxides (MgO, Al_2O_3, TiO_2, Cr_2O_3, Fe_2O_3, NiO, CuO, ZnO, ZrO_2, V_2O_5, MoO_3, $CoMoO_4$ and $NiMoO_4$) do not decompose SO_2 (12,13,16-26). Well-defined surfaces of oxides that expose metal cations with a high coordination number {MgO(100), ZnO(0001), TiO_2(110), NiO(001), V_2O_5(0001), Fe_2O_3(0001)} also do not dissociate SO_2 (17,18,27-31). Thus, stoichiometric oxides can be very good as sorbents (forming SO_3 or SO_4 species), but in general they will not be active as catalysts for reactions that involve S-O bond cleavage.

At a theoretical level, the bonding between SO_2 and the cations of oxides has been investigated using extended two-dimensional slabs {MgO, CaO, SrO, TiO_2 (21,24,32)}. In all the theoretical calculations, the frontier molecular orbitals of SO_2 mix poorly with electronic states located on the metal centers of the oxides. Figure 4 compares the band energies of a common oxide (MgO) and the molecular orbital energies of SO_2 (33,34). For the oxide, the empty and occupied bands are indicated by dotted and solid lines, respectively. The lowest unoccupied molecular orbital (LUMO) of SO_2 is S-O antibonding (32,34). In typical oxides, the occupied states of the metal centers are *too stable* for interacting or transferring electron density into the LUMO of SO_2 (i.e. no effective band-orbital mixing). This leads to small SO_2 adsorption energies on the cations and prevents dissociation of the molecule (21,24,32). To dissociate SO_2 on an oxide surface, one needs to create occupied metal states above the valence band of the

oxide. This can be accomplished by the introduction of O vacancies or other structural defects on the surface. This type of defects are frequent on oxide nanoparticles and tend to move upwards the occupied levels or downwards the empty levels (19), see Figure 4.

The presence of O vacancies in $CeO_2(111)$ and $Ce_{0.7}Zr_{0.3}O_2(111)$ induces the interaction of SO_2 with the metal cations and dissociation of the molecule (17,18). The right-side panel in Figure 5 shows S 2p photoemission results for the adsorption of SO_2 on several ceria systems (16). The left-panel displays the corresponding valence photoemission spectra for the ceria systems *before* the adsorption of SO_2 (16). In the case of CeO_2, the valence spectrum shows no signal in the region between 4 and 0 eV, where Ce^{3+} appears. The features between 8 and 4 eV contain O 2p character (main component) *and* metal character (16-18). On this system, the adsorption of SO_2 mainly produces SO_4 (16). O atoms can be preferentially removed from CeO_2 by Ar^+ sputtering (16-18). In Figure 5, the valence spectra for CeO_{2-x} and Ce_2O_{3+x} are characterized by a Ce^{3+} peak near 2 eV (16,17). Thus, the introduction of O vacancies creates occupied metal states above the valence band of CeO_2. This, phenomenon should make the oxide active for the dissociation S-O bonds (see above). And, indeed, the S 2p data exhibit features between 164 and 162 eV that come from the full decomposition of the SO_2 molecule on CeO_{2-x} and Ce_2O_{3+x}. CeO_2 is useful as a catalysts for the reduction of SO_2 by CO only at elevated temperatures, when CO is able to create O vacancies and associated Ce^{3+} sites in the oxide (16,33,35).

MgO(001), $TiO_2(110)$, NiO(001), $V_2O_5(0001)$ and $Fe_2O_3(0001)$ also become active for the decomposition of SO_2 after the creation of O vacancies by ion sputtering (21,27-32).

Theoretical calculations show that on these defects the adsorption energy of SO_2 is much larger than on flat stoichiometric surfaces with a substantial weakening and elongation of the S-O bonds (21,32). In principle, oxides that can be reduced by CO to form O vacancies, could be active catalysts for the $2CO_{gas} + SO_{2,gas} \rightarrow 2CO_{2,gas} + S_{ads}$ reaction. This is the case of CuO and CeO_2 (14,15,16,35). To favor the formation of O vacancies and active centers in these oxide, the reaction is usually carried out at high temperatures with a CO/SO_2 ratio in the feed $\exists$ 2. In the case of ceria, doping with a second metal helps the formation of O vacancies (36,37) and increases catalytic activity (14,15,35,38).

3. Chemistry of SO_2 and DeSOx processes on oxide nanoparticles

"Size effects" have not been studied for many oxides in a systematic way (39). For a vast number of oxide compounds, this comes out from the fact that the preparation procedures are not able to give a size distribution approaching the delta function (39). Detailed studies have appeared in the literature examining the interaction of SO_2 with only a few types of oxide nanoparticles: CaO, MgO, SrO, BaO, Al_2O_3, Al_2O_3/MgO, Fe_2O_3, Fe_2O_3/CaO, CeO_2 and $Ce_{1-x}Zr_xO_2$. The focus has been mainly on oxides of the alkaline-earth elements, frequently used as DeSOx scrubbers (11), and ceria based materials, useful as DeSOx catalysts (14,15).

3.1 Interaction with CaO, MgO and SrO

Nanoparticles of CaO, MgO, and SrO usually prefer to adopt a nearly perfect or somewhat distorted cubic shape, exposing the (100) face of a rocksalt crystal structure (40,41). Nanoparticles exhibiting (110) and (111) faces are much less common and frequently are not stable at high

temperatures. For example, when Mg metal is burned in air or oxygen, the MgO smoke particles that are formed are almost perfect cubes having (100) faces (42). Special procedures to prepare MgO nanoparticles exhibiting (110) and (111) faces have been partially successful (43), but in general they tend to facet to surfaces containing (100) planes (44).

An important aspect to consider when dealing with MgO nanoparticles is the possible presence of O vacancies (45). These can have a tremendous influence on the electronic and chemical properties of the nanoparticles. The anionic vacancies in MgO are known as F centers; depending on the charge one can have F, F^+, and F^{2+} centers which correspond to the removal of a neutral O atom, of an O^- or of an O^{2-} anion, respectively (45). The F centers can be described as an electron pair trapped in the cavity left by the missing oxygen. They can produce electronic states localized well above the valence band of MgO (45). The F^+ centers consist of a single electron associated with the vacancy and give rise to a typical signal in EPR. Finally, F^{2+} centers are strongly electron deficient and have a tendency to ionize bonded molecules.

The adsorption of SO_2 on nanoparticles of MgO at 300 K mainly produces SO_4 groups, $SO_2(gas) + 2O(oxide) \rightarrow SO_4(adsorbed)$, with a very small amount of SO_3 and without cleavage of S-O bonds (i.e. no deposition of atomic sulfur on the Mg cations) (44). In contrast, the adsorption of SO_2 on a MgO(100) crystal under similar conditions mainly yields SO_3 with SO_4 as a secondary product (see above) (44). Calculations based on the Hartree-Fock method and DFT indicate that the formation of SO_4 on MgO(100) in not spontaneous and requires a major reconstruction of the surface with the participation of defect sites (21,24). In the calculations, the interaction of SO_2 with MgO(100) produces a SO_3-like species (21,24). For SO_2 on the MgO nanoparticles, the existence of corner and edge sites in the oxide substrate facilitates the structural changes necessary for the

formation of SO_4 (46).

For several industrial applications MgO is doped with small amounts of a transition metal. Such doping can induce structural transformations and be used to stabilize MgO nanoparticles that expose (110) or (111) faces (44) The doping also can lead to perturbations in the electronic properties of the nanoparticles by favoring the formation of O vacancies or by introducing new occupied states above the valence band of MgO as shown in Figure 6 (47). The position of the new occupied states depends on the nature of the dopant element. This phenomenon is particularly important when the doping is done with metals like Fe or Cr that induce states 2-3 eV above the MgO valence band. In general, the $TM_xMg_{1-x}O$ systems (TM= Ni, Fe, Mn, Cr) exhibit electronic and chemical properties different from those of pure MgO (44,47).

The doping of the MgO nanoparticles with Cr produces a system that is extremely efficient for the destruction of SO_2 (44,48). The $Mg_{1-x}Cr_xO_2$ nanoparticles are able to cleave the S-O bonds at temperatures below 300 K, while bulk MgO and Cr_2O_3 only adsorb the molecule to form SO_3 or SO_4 species (44,48). The Cr atoms in the $Mg_{1-x}Cr_xO_2$ nanoparticles are trapped in a "+2" formal oxidation state and have occupied electronic states that appear well above the MgO valence band (see Figure 6). These properties facilitate interactions with the LUMO of SO_2 and make the nanoparticles more chemically active than bulk MgO or Cr_2O_3 (44,48).

Depending on the exact procedure followed for the preparation, nanoparticles of MgO and CaO with polyhedral or hexagonal shapes can be prepared, but they also contain OH groups (40,49). In these morphological shapes, the nanoparticles posses more defects than expected for the typical cubic shape of MgO and CaO (49). Such defects could be of the Frenkel or Schottky type (vacancies), or be manifested as unusual configurations of edges, corners, or crystal planes (40).

Adsorption data for SO_2 and other molecules are conclusive that the polyhedral or hexagonal nanocrystals of MgO and CaO are more reactive than cubic microcrystals of these oxides (49). This has been mainly attributed to morphological differences, including the concentration of defects. However, intrinsic electronic effects due purely to "smallness" (confinement) could not be ruled out (49).

A comparison of the reactivity of CaO particles with sizes of 7.3 and 14.6 nm shows that the smaller particles are ~ 1.5 times more efficient for the trapping of SO_2 than the bigger particles (50). This can be attributed to a larger concentration of corner and edge sites in the 7.3 nm particles; sites which are important for the adsorption of SO_2 (51). Both sizes of CaO nanoparticles are more reactive than the bulk oxide. Furthermore, the pure nanoparticles of CaO exhibit a higher activity for S-O bond cleavage than nanoparticles of pure MgO (44,50,51). A mixture of calcium sulfite, calcium sulfate and calcium sulfide is observed on the CaO upon the adsorption of SO_2. These species may be formed through two different mechanisms (50)

$$CaO + SO_2 \rightarrow CaSO_3 \qquad (3)$$

$$CaO + SO_2 \rightarrow \tfrac{3}{4}\, CaSO_4 + \tfrac{1}{4}\, CaS \qquad (4)$$

The SO_2/CaO system is complex and cation-to-cation exchanges of the $SO_3^{2-} \leftrightarrow O^{2-}$, $SO_4^{2-} \leftrightarrow O^{2-}$ and $S^{2-} \leftrightarrow O^{2-}$ type may be occurring (50). One reason why the nanocrystals display such a large efficiency for trapping SO_2 is that the small size of the particles permits a shorter ion migration distance to the core of the particle than for that of conventional calcium oxide. With the shorter ion migration distances it is easier to react with the entire CaO particle by effectively "eating out" the core (50).

Nanoparticles of SrO also can be used to mitigate atmospheric pollution and sequester SO_2

(52). A particularly large efficiency was seen for nanoparticles with sizes under 10 nm. The results of EXAFS indicate that this large efficiency is associated with a substantial degree of disorder in the lattice structure (52).

3.2 Interaction with Al_2O_3 and Al_2O_3/MgO

Nanocrystals of Al_2O_3 and Al_2O_3/MgO were produced through a modified aerogel synthesis (53). The resulting oxides were in the form of powders having crystallites of about 2 nm or less in dimension. They exhibited a reactivity towards SO_2 much larger than that of bulk aluminas or MgO (53). This is thought to be due to morphological differences, whereas larger crystallites have only a small percentage of reactive sites on the surface, smaller crystallites posses much higher surface concentration of such sites per unit surface area.

Figure 7 shows infrared spectra collected after exposing the nanoparticles (NC) and commercial powders (CM) to SO_2 (20 Torr, room temperature) followed by a 2 hour evacuation (53). The CM-MgO and CM-Al_2O_3 showed no adsorbed species. On the other hand, both NC-Al_2O_3 and NC-Al_2O_3/MgO show new peaks at 1135 and 1130 cm^{-1} that correspond to chemisorbed monodentate SO_2. Clearly the nanoparticles have a special chemical activity. The nanoparticles of Al_2O_3/MgO were found to be the best SO_2 sorbents among the examined samples (53). A significant feature is that, by a cogellation synthesis, Al_2O_3 and MgO have been intermingled, which engenders enhanced reactivity/capacity over the pure forms of nanoscale Al_2O_3 or MgO (53).

3.3 Interaction with Fe_2O_3, Fe_2O_3/CaO, and Fe_2O_3/SrO

Nanoparticles of Fe_2O_{3-x} with sizes in the range of 2-4 nm can be used for sequestering SO_2

and do have a moderate activity for the $SO_2 + 2CO \rightarrow 2CO_2 + S_n$ reaction (3,44). S K-edge spectra taken after the adsorption of SO_2 at room temperature point to the presence of S, SO_2 and SO_3 on the surface of the Fe_2O_{3-x} nanoparticles (44). They are much more reactive than bulk Fe_2O_3 (3,44), probably due to the presence of O vacancies and surface defects (44). Measurements of X-ray powder diffraction show a lot of stress, caused by imperfections, in the lattice of the Fe_2O_{3-x} nanoparticles (44).

Coating with Fe_2O_3 enhances the ability of CaO and SrO nanoparticles to adsorb SO_2 (50,52, 54). Only small amounts of Fe_2O_3 are necessary in order to see this phenomenon (see Figure 8). The supported Fe_2O_3 acts as a facilitator and there is a direct reaction of the calcium or strontium oxide with SO_2 The reaction does not stop at the surface, and the CaO and SrO behave as a stoichiometric reagents (50,54). Table 1 compares the reaction efficiencies for the trapping of SO_2 by calcium oxide nanoparticles pure or coated with Fe_2O_3 (50). The CaO nanoparticles have sizes of 7.3 and 14.6 nm (SP and MP particles, respectively, in our notation). The extent of the reaction is indicated by the breakthrough number and the number of moles of SO_2 that are adsorbed per mole of CaO (50). The breakthrough number is defined as the number of 1-mL injections that are made to the reaction cell until the first trace of excess SO_2 is eluted from the bed of the adsorbent. In Table 1, it is obvious the tremendous effect of Fe_2O_3 on the efficiency of the system. MP-CaO particles coated with Fe_2O_3 are more active than SP-CaO particles, and when the SP-CaO particles are coated with Fe_2O_3 the efficiency of the system is very close to the maximum limit (i.e. 0.94 versus 1.0). Systematic studies indicate that the enhancement in reactivity is a kinetic phenomenon (50).

The structure of Fe_2O_3/SrO nanoparticles before and after exposure to SO_2 was investigated using Sr and Fe K-edge EXAFS measurements (52). In the fresh Fe_2O_3/SrO nanoparticles, the first

Sr-O peak is almost unchanged with respect to that in bulk SrO, but the second Sr-Sr peak is dramatically decreased. This points to a disordered oxide lattice in the Fe_2O_3/SrO nanoparticles and may help to enhance their reactivity towards SO_2 (52). The Fe K-edge EXAFS data for the fresh Fe_2O_3/SrO nanoparticles indicate that the Fe_2O_3 coating has a large degree of disorder and some of the cations may be reduced to metallic iron (52). Upon interaction with SO_2, the characteristic Fe-S peak for iron sulfide was not seen. Unfortunately, it was not possible to discriminate between disordered Fe_2O_3 and $Fe_2(SO_4)_3$ because they have a similar first Fe-O peak (52).

3.4 Interaction with CeO_2 and doped-ceria

Figure 1 compares S K-edge XANES spectra collected after dosing SO_2 at 25 ^oC to $CeO_2(111)$ and $Ce_{0.7}Zr_{0.3}O_2(111)$ surfaces and nanoparticles of CeO_2, $Ce_{0.66}Zr_{0.33}O_2$ and $Ce_{0.66}Ca_{0.33}O_{2-y}$ (19). The spectra for the extended surfaces display a peak for SO_4 as a dominant feature with a minor peak for SO_3. For the oxide nanoparticles, again one finds that SO_4 is the main sulfur-containing species present on the surface but, in addition, features are seen at photon energies between 2470 and 2472 eV that denote the existence of metal-S bonds (19) as a consequence of the full dissociation of sulfur dioxide ($SO_2 \rightarrow S + 2O$) on the cerium cations. In principle, clusters and nanoparticles of $Ce_{1-x}Zr_xO_2$ probably have metal cations at corner and edge sites that can interact well with the SO_2 molecule. On some of these special sites that are very reactive SO_2 decomposes. In addition, there may be O vacancies in the surface of the $Ce_{0.66}Zr_{0.33}O_2$ and $Ce_{0.66}Ca_{0.33}O_{2-y}$ nanoparticles that facilitate S-O bond cleavage (36). In Figure 1, the $Ce_{0.66}Ca_{0.33}O_{2-y}$ system has the largest concentration of O vacancies (36), and the highest reactivity for the dissociation of SO_2.

From the XRD data of the nanoparticles, one can get a strain parameter that is a measurement of the lattice stress existing in the materials because of surface defects (differences in local symmetry and distances with respect to the bulk) and/or the crystal imperfections (O vacancies, other point defects, line defects and plane defects) (36,37,39). The top panel in Figure 8 shows the strain parameters for the CeO_2, $Ce_{0.66}Zr_{0.33}O_2$ and $Ce_{0.66}Ca_{0.33}O_{2-y}$ nanoparticles (36,37). Pure ceria nanoparticles exhibit a larger lattice strain than bulk ceria (36). Clearly, the introduction of an alien species like Zr or Ca leads to extra forces that increase the strain in the lattice of the nanoparticles. The effects of Ca are more significant because Ca likes to form oxides with a relatively low content of O and the oxidation states of Ca and Ce are different (36). In Figure 8 a qualitative correlation can be found between the amount of S deposited on the nanoparticles, as a consequence of the dissociation of SO_2 (19), and the strain parameter of the nanoparticles. The nanoparticles that have more lattice imperfections, $Ce_{0.66}Ca_{0.33}O_{2-y}$, are the more active for S-O bond cleavage.

Figure 9 shows the effect of the temperature on the sulfate (SO_4) signal for the CeO_2 and $Ce_{1-x}Zr_xO_2$ systems in Figure 1 (19). As the temperature is raised SO_4 decomposes. In the case of the CeO_2(111) and $Ce_{0.7}Zr_{0.3}O_2$(111) surfaces, the adsorbed SO_4 transforms into SO_2 gas. On the other hand, in the case of the nanoparticles, most of the decomposed SO_4 yields SO_2 gas, but a fraction undergoes complete decomposition depositing S on the oxide substrate. The SO_4 adsorbed on the nanoparticles is somewhat more stable than that present on the (111) surfaces. For both types of systems, the presence of Zr seems to induce an increase in the thermal stability of the adsorbed sulfate. The Zr cations also enhance the thermal stability of SO_4 species formed on partially reduced $Ce_{1-x}Zr_xO_{2-y}$(111) surfaces (17).

Nanoparticles of $Ce_{1-x}D_xO_{2-y}$ (D= Sr, Sc, La, Gd, Ni, Cu) display catalytic activity for the reduction of SO_2 with carbon monoxide ($SO_2 + 2CO \rightarrow 2CO_2 + S$) or methane ($2SO_2 + CH_4 \rightarrow CO_2 + 2H_2O + 2S$) (55,56). High catalytic activity was observed when ceria was doped with copper or nickel. It is well established that copper facilitates the reduction of ceria nanoparticles by CO (57). A redox mechanism has been proposed to explain the reduction of SO_2 by CO on the $Ce_{1-x}D_xO_{2-y}$ nanoparticles (55)

$$\text{cat-O} + CO \rightarrow \text{cat-[ ]} + CO_2 \qquad (5)$$

$$\text{cat-[ ]} + SO_2 \rightarrow \text{cat-O} + SO \qquad (6)$$

$$\text{cat-[ ]} + SO \rightarrow \text{cat-O} + S \qquad (7)$$

First, an oxygen vancancy is created as a surface capping oxygen is removed by CO. Then, SO_2 donates one of its oxygens to the vacancy to form SO. The SO is mobile on the surface until it finds another vacancy to donate its oxygen or a vacancy may migrate to a neighboring site to accept its oxygen. High oxygen mobility in the catalyst will facilitate the oxygen transfer from one site to another on the surface or from the bulk to the surface. A dopant may help in this respect. However, surface reduction by CO is still the key step to initiate the reaction (55). Under reaction conditions, CO and SO_2 compete for the surface oxygen. Reaction with CO produces an O vacancy, equation (5), while reaction of SO_2 with the surface oxygens forms sulfite or sulfate species that are strongly bound and hinder the redox reaction.

The Cu-Ce(La)-O nanocatalysts displayed a better performance than Ce(La)-O_2 or CuO (55). Thus, a synergistic effect was observed for the Cu-dopped ceria. Copper and cerium oxide probably play different roles in the redox mechanism (55). Cerium oxide comprises the matrix of the catalyst and provides the oxygen and oxygen vacancy sources, while Cu cations promote the

reducibility of cerium oxide and provide surface sites for CO adsorption (55,57).

4. Conclusions

On bulk stoichiometric oxides, SO_2 mainly reacts with the O centers to form SO_3 or SO_4 species that decompose at elevated temperatures. Adsorption on the metal cations occurs below 300 K and does not lead to cleavage of the S-O bonds. In bulk oxides, the occupied cation bands are too stable for effective bonding interactions with the LUMO of SO_2. The effects of quantum confinement on the electronic properties of oxide nanoparticles and the structural defects that usually accompany these systems in general favor the bonding and dissociation of SO_2. Thus, nanoparticles of MgO, CaO, SrO, Al_2O_3, Fe_2O_3 and CeO_2 are all more efficient for sequestering SO_2 than the corresponding bulk oxides. Structural imperfections in pure or metal-doped ceria nanoparticles accelerate the reduction of SO_2 by CO by facilitating the formation and migration of O vacancies in the oxide surface.

Acknowledgements

The author is grateful for the financial support by the US Department of Energy (Divisions of Chemical and Materials Science) under contract DE-AC02-98CH10086.

REFERENCES

1. Adlkofer, J. ***Handbook of Heterogeneous Catalysis*****;** Ertl, G., Knözinger, H., and J. Weitkamp, J. (Editors), (Wiley-VCH, New York, 1997) Volume 4, p. 1776.
2. Stern, A.C., Boubel, R.W., Turner, D.B., and Fox, D.L. ***Fundamentals of Air Pollution,*** 2nd ed. (Academic Press: Orlando, FL, 1984).
3. Piéplu, A., Saur, O., Lavalley, J.-C., Legendre, O. and Nédez, C. ***Catal. Rev. -Sci. Eng.*** 40: 409, 1998**.**
4. ***Environmental Catalysis,*** Armor, J.N. (Editor), ACS Symposium Series No 552 (American Chemical Society: Washington DC, 1994).
5. Shelef, M., and McCabe, R.W. ***Catal. Today*** 62:35, 2000
6. Bartholomew, C.H., Agrawal, P.K., and Katzer, J.R. ***Adv. Catal***. 31: 135, 1982.
7. Rodriguez, J.A. and Hrbek, J. ***Accounts of Chemical Research***, 32:719, 1999.
8. Beck, D.D., Sommers, J.W., and DiMaggio, C.L. ***Appl. Catal. B*** 11:273, 1997.
9. Beck, D.D. ***Catalyst Deactivation*** 111:21, 1997.
10. Gorte, R. private communication.
11. Slack, A.V., and Holliden, G.A. ***Sulfur Dioxide Removal from Waste Gases***, 2nd Edition (Noyes Data Corporation: Park Ridge, NJ 1975).
12. Centi, G., Passarini, N., Perathoner, S. and Riva, A. ***Ind. Eng. Chem. Research***, 31:1947 , 1992.
13. Waqif, M., Saur, O., Lavalley, J.C., Perathoner, S. and Centi, G. ***J. Phys. Chem***. 95:4051, 1991.
14. Zhu, T., Kundakovic, K., Dreher, A., Flytzani-Stephanopoulos, M. ***Catal. Today***,

50:381, 1999.

15. Liu, W., Wadia, C., and Flytzani-Stephanopoulos, M. ***Catal. Today***, 28: 391, 1996.

16. Rodriguez, J.A., Jirsak, T., Freitag, A., Hanson, J.C., Larese, J.Z., and Chaturvedi, S. ***Catal. Lett.*** 62:113, 1999.

17. Liu, G., Rodriguez, J.A., Chang, Z., Hrbek, J., Peden, C.H.F. *J. Phys. Chem B*, 108:2931 (2004).

18. Overbury, S.H., Mullins, D.R., Huntley, D., Kundakovic, L.J. *J. Phys. Chem. B*, 103:11308 (1999).

19. Rodriguez, J.A., Wang, X., Liu, G., Hanson, J.C., Hrbek, J., Peden, C.H.F., Iglesias-Juez, A., Fernández-García, M. *J. Molec. Catal. A: Chemical*, 228:11 (2005).

20. Rodriguez, J.A., Pérez, M., Jirsak, T., González, L., and Maiti, M. ***Surf. Sci.*** 477: L279, 2001.

21. Rodriguez, J.A., Jirsak, T., Freitag, A., Larese, J.Z. and Maiti, A. ***J. Phys. Chem. B***, 104:7439, 2000.

22. Rodriguez, J.A., Jirsak, T., Chaturvedi, S. and Kuhn, M. ***Surf. Sci.*** 442:400, 1999.

23. Rodriguez, J.A., Jirsak, T., Chaturvedi, S. and Dvorak, J. ***J. Molecular Catalysis A***, 167:47, 2001.

24. Schneider, W.F., ***J. Phys. Chem. B***, 108:273, 2004.

25. Waqif, M., Saad, A.M., Bensitel, M., Bachelier, J., Saur, O., and Lavalley, J.C. ***J. Chem. Soc., Faraday Trans.*** 88:2931, 1992**.**

26. Rodriguez, J.A., Hanson, J.C., Chaturvedi, S., and Brito, J.L. ***Studies in Surf. Sci.***

Catal. 130:2795, 2000.

27. Warburton, D.R., Pundie, D., Muryn, C.A., Prahakaran, K., Wincott, P.L., and Thorton, G. ***Surf. Sci.*** 269/270:305, 1992.

28. Muryn, C., Purdie, D., Hardman, P., Johnson, A.L., Prakash, N.S., Raiker, G.N., Thorton, G., and Law, D. ***Faraday Discuss. Chem. Soc.*** 89:77, 1990.

29. Kurtz, R.L., and Henrich, V.E. ***Phys. Rev. B*** 36:3413, 1987.

30. Zhang, Z., and Henrich, V.E. ***Surf. Sci.*** 225:47, 1990.

31. Li, X., and Henrich, V.E. ***Phys. Rev. B***, 48:17486, 1993.

32. Rodríguez, J.A., Liu, G., Jirsak, T., Hrbek, J., Chang, Z., Dvorak, J., Maiti, A. *J. Am. Chem. Soc.* 124:5242, 2002.

33. Rodriguez, J.A., Jirsak, T. and Hrbek, J. ***J. Phys. Chem. B***, 103:1966, 1999.

34. Rodriguez, J.A., Chaturvedi, S., Kuhn, M. and Hrbek, J. ***J. Phys. Chem. B***, 102:5511, 1998.

35. Tschope, A., Liu, W., Flytzani-Stephanopoulos, M. and Ying, J.Y. ***J. Catal.*** 157:42, 1995.

36. Rodríguez, J.A., Wang, X., Hanson, J.C., Liu, G., Iglesias-Juez, A., Fernández-García, M., *J. Chem. Phys.* 119:5659, 2003.

37. Wang, X., Hanson, J.C., Liu, G. Rodriguez, J.A., Iglesias-Juez, A., Fernández-García, M., *J. Chem. Phys.* 121:5434, 2004.

38. de Carolis, S., Pascual, J.L., Petterson, L.G.M., Baudin, M., Wojcik, M., Hermansson, K., Palmqvist, A.E.C. and Muhammed, M. ***J. Phys. Chem. B***, 103:7627, 1999.

39. Fernández-García, M., Martínez-Arias, A., Hanson, J.C., Rodríguez, J.A. *Chem. Rev.* 104:4063, 2004.

40. Klabunde, K.J., Stark, J., Koper, O., Mobs, C., Park, D.G., Decker, S., Jiang, Y., Lagadic, I., Zhang, D. *J. Phys. Chem.* 100: 12142, 1996.

41. Tasker, P.W. *Adv.* in *Ceramics,* 10:176, 1984.

42. Moodie, A.F., Warble, C.E. *J. Crystal Growth*, 10:26, 1971.

43. Mackrodt, W.C., Tasker, P.W. *Chem. Britain*, 21:13, 1985.

44. DeSantis, E., Ferrari, J. private communication.

45. Pacchioni, G., Pescarmona, P. *Surf. Sci.* 412/413: 657, 1998.

46. Pacchioni, G., Clotet, A., Ricart, J.M. *Surf. Sci.* 315:337, 1994.

47. Rodriguez, J.A. *Catal. Today,* 85: 177, 2003.

48. Rodriguez, J.A., Jirsak, T., Pérez, M., Chaturvedi, S., Kuhn, M., González, L., Maiti, A. *J. Am. Chem. Soc.* 122:12362, 2000.

49. Lucas, E., Decker, S., Khaleel, A., Seitz, A., Futlz, S., Ponce, A., Li, W., Carnes, C., Klabunde, K.J. *Chem. Eur. J.* 7: 2505, 2001.

50. Decker, S., Klabunde, K.J., *J. Am. Chem. Soc.* 118:12465, 1996.

51. Pacchioni, G., Ricart, J.M., Illas, F. *J. Am. Chem. Soc.* 116: 10152, 1994.

52. Moscovici, J., Michalowicz, A., Decker, S., Lagadic, I., Latreche, K., Klabunde, K. *J. Synchrotron Rad.* 6:604, 1999.

53. Carnes, C.L., Kapoor, P.N., Klabunde, K.J. *Chem. Mater.* 14:2922, 2002.

54. Decker, S.P., Klabunde, J.S., Khaleel, A., Klabunde, K.J. *Environ. Sci. Technol.* 36:762, 2002.

55. Liu, W., Wadia, C., Flytzani-Stephanopoulos, M. *Catal. Today* 28:391, 1996.

56. Flytzani-Stephanopoulos, M., Zhu, T., Li, Y. *Catal. Today* 62:145, 2000.

57. Wang, X., Rodriguez, J.A., Hanson, J.C., Gamarra, D., Martínez-Arias, A., Fernández-García, M. *J. Phys. Chem. B*, 110:428, 2006.

Table 1 : Breakthrough Numbers an Reaction Efficiencies for the Trapping of SO_2 by CaO and Fe_2O_3/CaO nanoparticles.[a]

Sample	Breakthrough number	Reaction efficiencies (mol of SO_2/mol of CaO)[b]
MP-CaO[c]	11	0.36
Fe_2O_3/MP-CaO	23	0.55
SP-CaO[d]	19	0.51
Fe_2O_3/SP-CaO	44	0.94

[a] From ref (48) [b] Theoretical maximum would be 1.0
[c] MP= 14.6 nm in size [d] SP= 7.3 nm in size

Figure Captions

Fig 1 S K-edge spectra taken after dosing SO_2 to $CeO_2(111)$ and $Ce_{0.7}Zr_{0.3}O_2(111)$ surfaces, and nanoparticles of CeO_2, $Ce_{0.66}O_{0.33}O_2$ and $Ce_{0.66}Ca_{0.33}O_{2-y}$. The samples were exposed to 0.1 Torr of SO_2, for 5 min at 25 ^oC (from ref. 19).

Fig 2 Top and side views of an oxygen-terminated $Ce_{1-x}Zr_xO_2(111)$ surface ($x < 0.4$). The large spheres represent O atoms, and the small spheres correspond to Ce or Zr atoms in a solid solution.

Fig 3 S 2p photoemission spectra for the adsorption of SO_2 on a MgO(100) single crystal and a MgO(100) epitaxial film grown on a Mo(100) substrate (from ref. (20)).

Fig 4 Energy position for the valence and conduction bands of bulk MgO. Empty states are shown as doted lines, while solid lines denote occupied states. For comparison, we also include the molecular orbital energies of SO_2, and the type of energy shift that can occur for the states of a nanoparticle. Such a shift facilitates interactions with the LUMO of SO_2. The zero of energy is the vacuum level (from refs. (33,34).

Fig 5 Right-side: Valence photoemission spectra for a series of ceria systems. Left-side: S 2p spectra taken after dosing 5 langmuir of SO_2 at 300 K to the ceria surfaces (from ref. (19)).

Fig 6 Valence photoemission spectra for pure and doped magnesium oxide (from refs. 39,48).

Fig 7 Infrared spectra collected after exposing nanoparticles of Al_2O_3 and Al_2O_3/MgO to 20 Torr of SO_2 at room temperature followed by a two 2 hour evacuation. “NC” and

"CM" refer to nanocrystalline and commercial, respectively (from ref. (53)).

Fig 8 Top panel: Lattice strain for CeO_2, $Ce_{0.66}Zr_{0.33}O_2$ and $Ce_{0.66}Ca_{0.33}O_{2-y}$ nanoparticles (36,37). Bottom panel: Amount of atomic sulfur deposited on CeO_2, $Ce_{0.66}Zr_{0.33}O_2$ and $Ce_{0.66}Ca_{0.33}O_{2-y}$ nanoparticles as a consequence of the dissociation of SO_2. The The samples were exposed to 0.1 Torr of SO_2, for 5 min at 25 ^oC. Then, the gas was evacuated and S K-edge spectra were collected (from ref. 19).

Fig 9 Effect of temperature on the XANES signal for the SO_4 formed on the CeO_2 and $Ce_{1-x}Zr_xO_2$ systems of Figure 1. The top panel shows the results for the (111) surfaces, while the bottom panel contains the corresponding results for the nanoparticles (from ref 19).

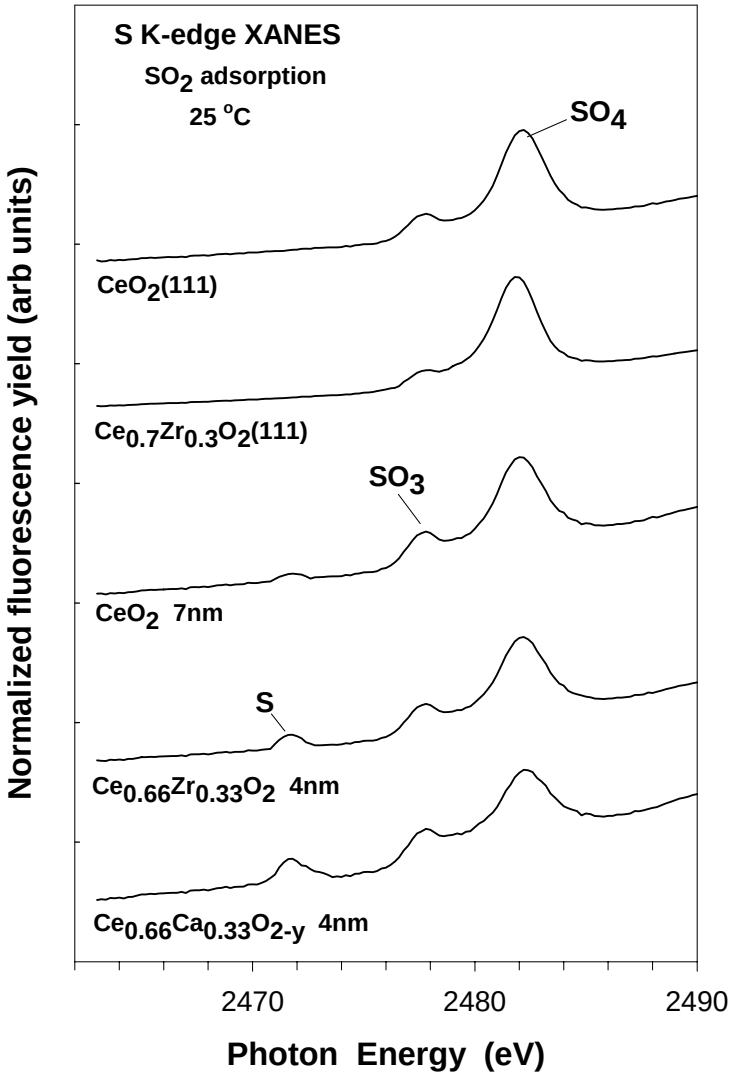
S K-edge XANES
SO2 adsorption
25 °C
SO4
CeO2(111)
Ce0.7Zr0.3O2(111)
SO3
CeO2 7nm
S
Ce0.66Zr0.33O2 4nm
Ce0.66Ca0.33O2-y 4nm
Normalized fluorescence yield (arb units)
2470
2480
2490
Photon Energy (eV)

Fig. 1

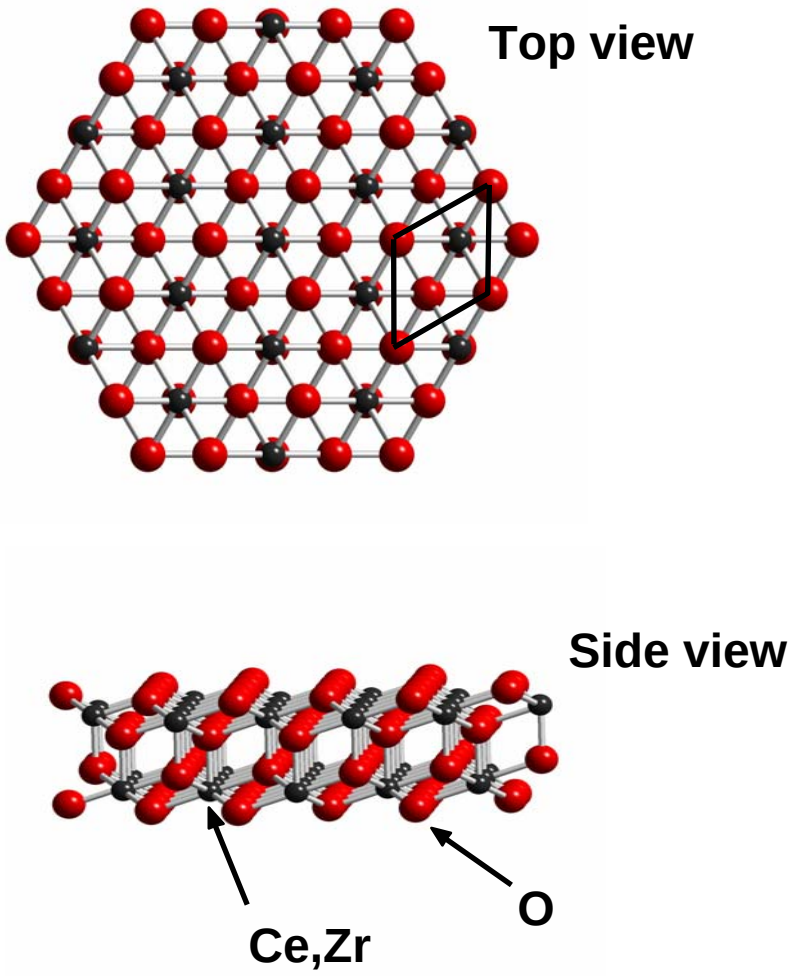

Fig. 2

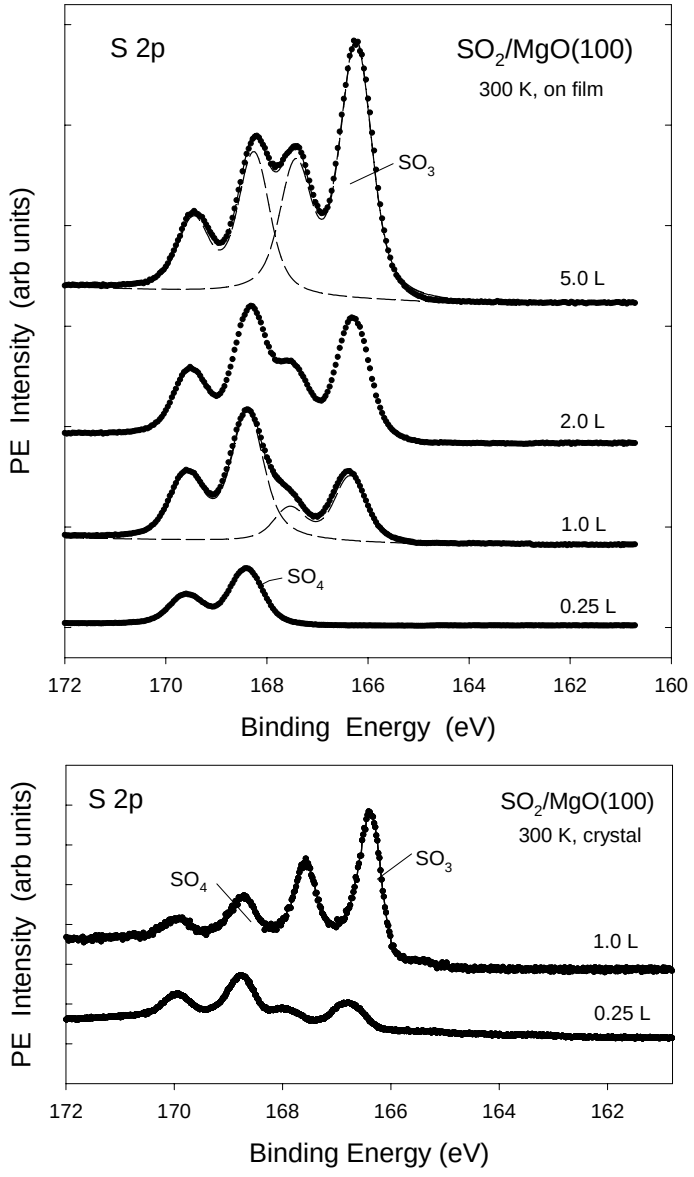
S 2p
SO2/MgO(100)
300 K, on film
SO3
5.0 L
2.0 L
1.0 L
SO4
0.25 L
PE Intensity (arb units)
172
170
168
166
164
162
160
Binding Energy (eV)
S 2p
SO2/MgO(100)
300 K, crystal
SO4
SO3
1.0 L
0.25 L
PE Intensity (arb units)
172
170
168
166
164
162
Binding Energy (eV)

Fig. 3

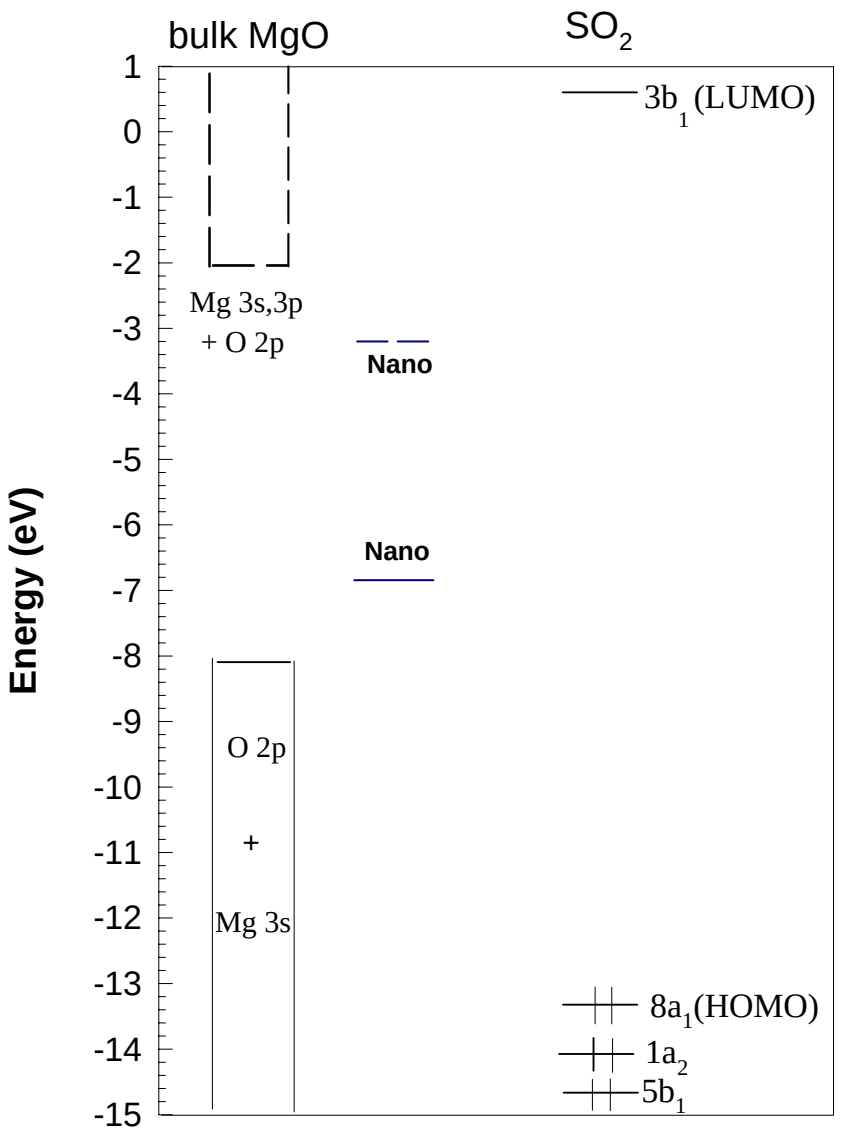
bulk MgO
SO2
Energy (eV)
1
0
-1
-2
-3
-4
-5
-6
-7
-8
-9
-10
-11
-12
-13
-14
-15
3b1 (LUMO)
Mg 3s,3p
+ O 2p
Nano
Nano
O 2p
+
Mg 3s
8a1(HOMO)
1a2
5b1

Fig. 4

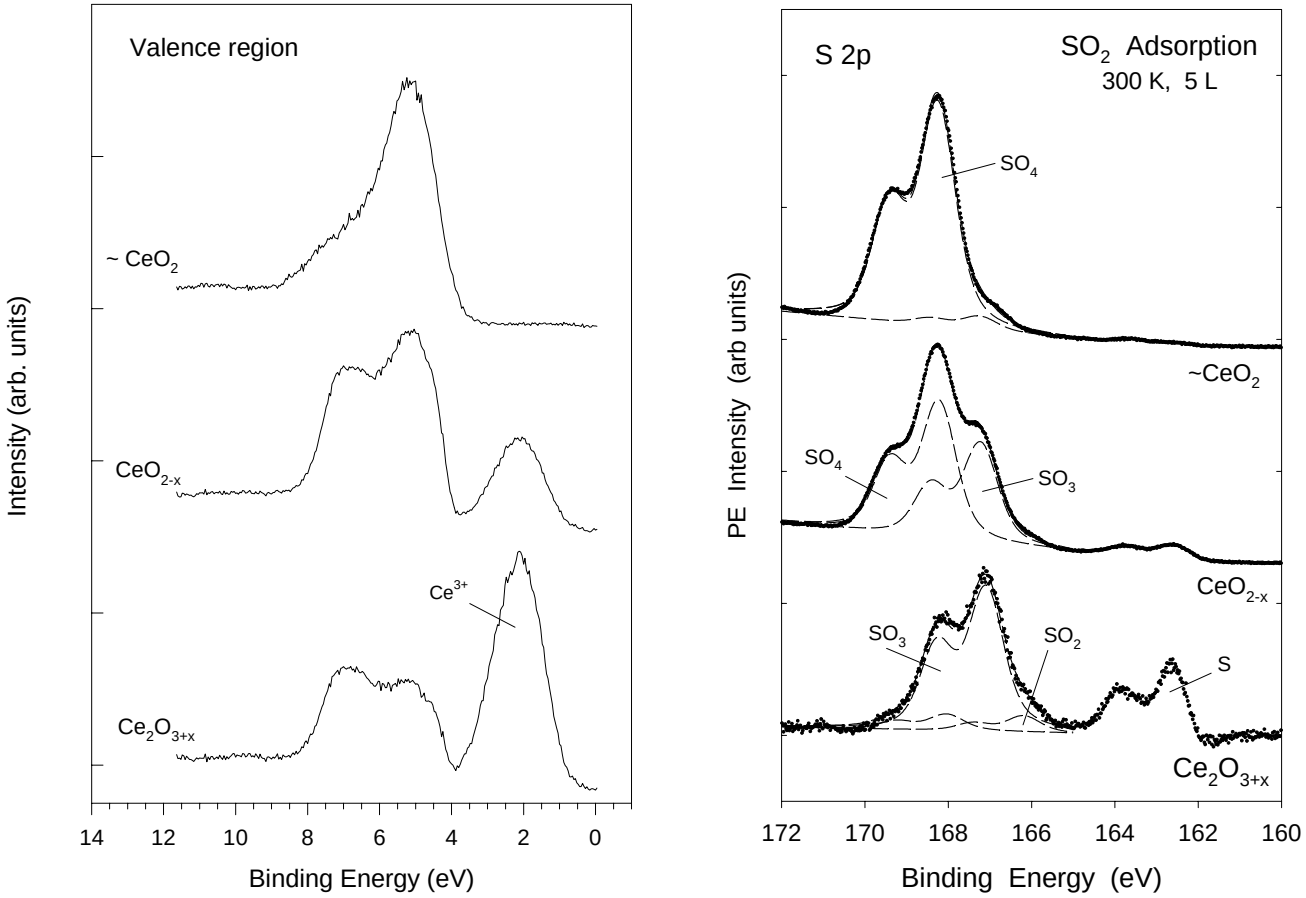
Valence region
~ CeO2
CeO2-x
Ce3+
Ce2O3+x
Intensity (arb. units)
14
12
10
8
6
4
2
0
Binding Energy (eV)
S 2p
SO2 Adsorption
300 K, 5 L
SO4
~CeO2
SO4
SO3
CeO2-x
SO3
SO2
S
Ce2O3+x
PE Intensity (arb units)
172
170
168
166
164
162
160
Binding Energy (eV)

Fig. 5

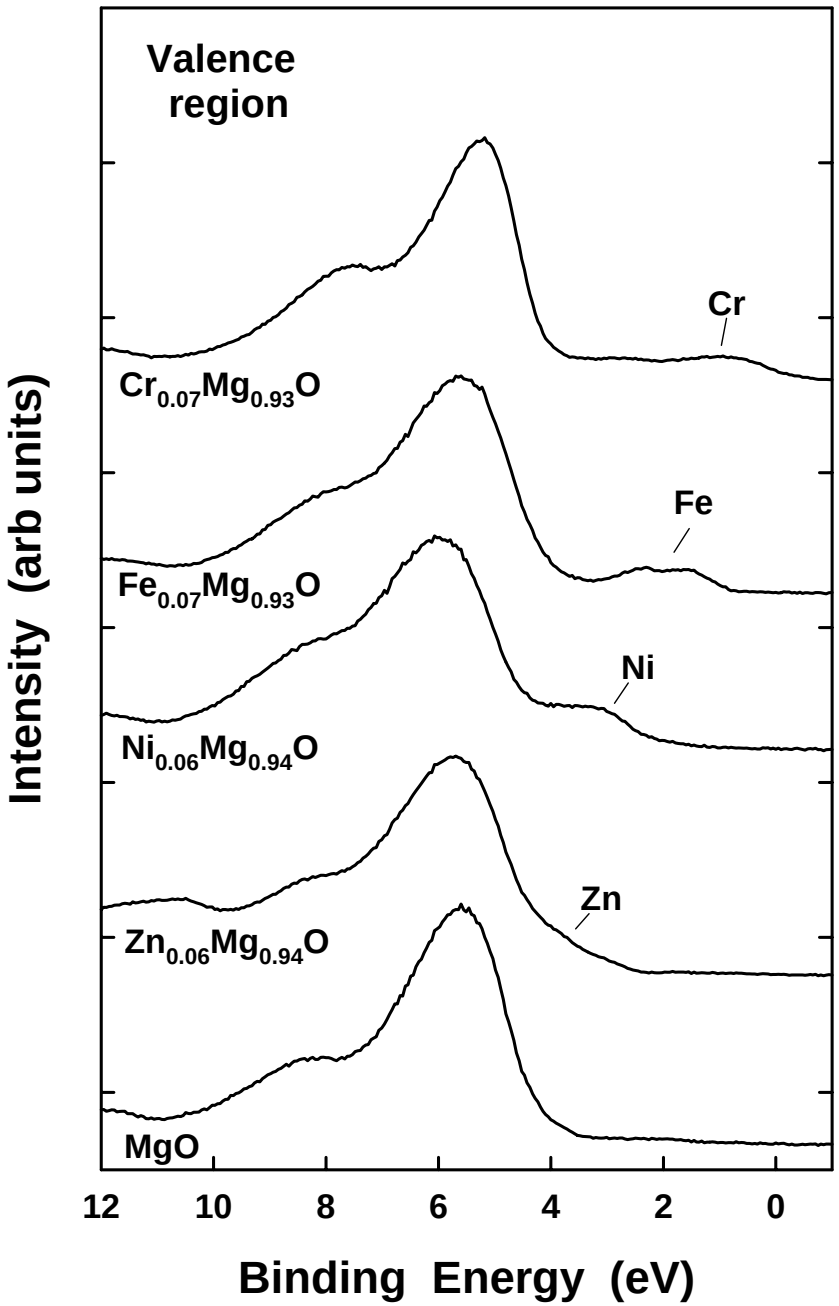
Valence
region
Cr
Cr0.07Mg0.93O
Fe
Fe0.07Mg0.93O
Ni
Ni0.06Mg0.94O
Zn
Zn0.06Mg0.94O
MgO
Intensity (arb units)
12
10
8
6
4
2
0
Binding Energy (eV)

Fig. 6

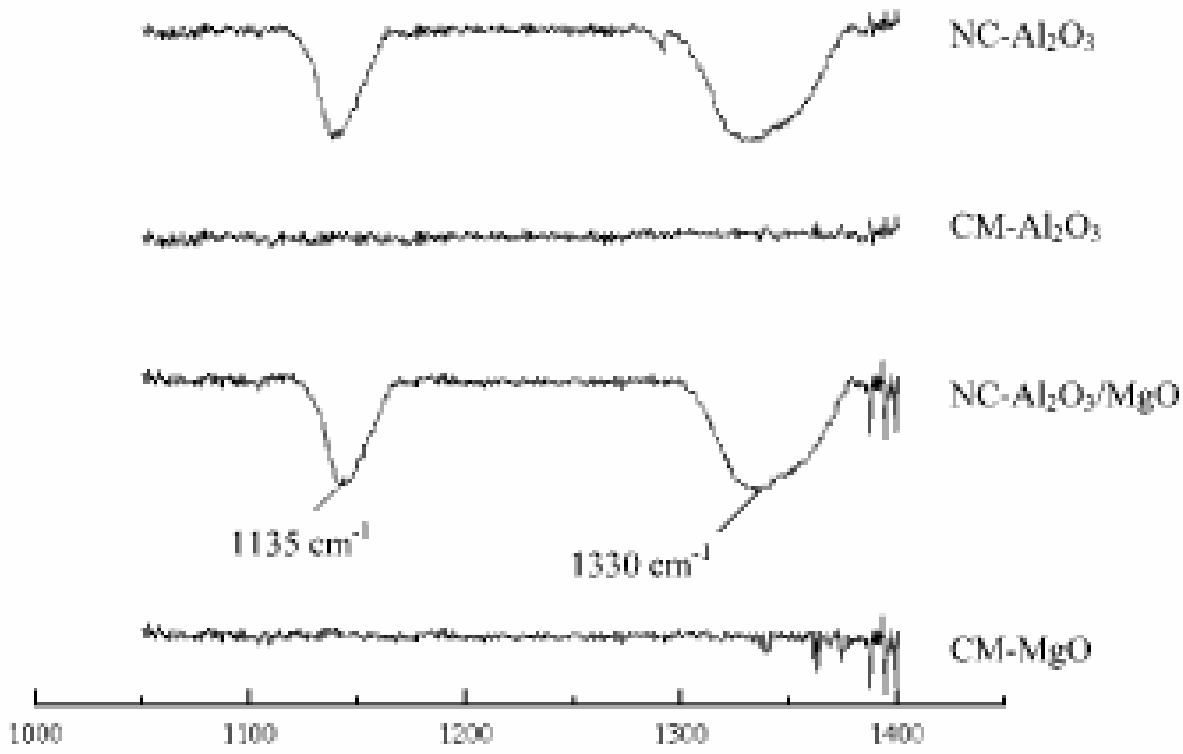
NC-Al2O3
CM-Al2O3
NC-Al2O3/MgO
1135 cm-1
1330 cm-1
CM-MgO
1000
1100
1200
1300
1400

Fig. 7

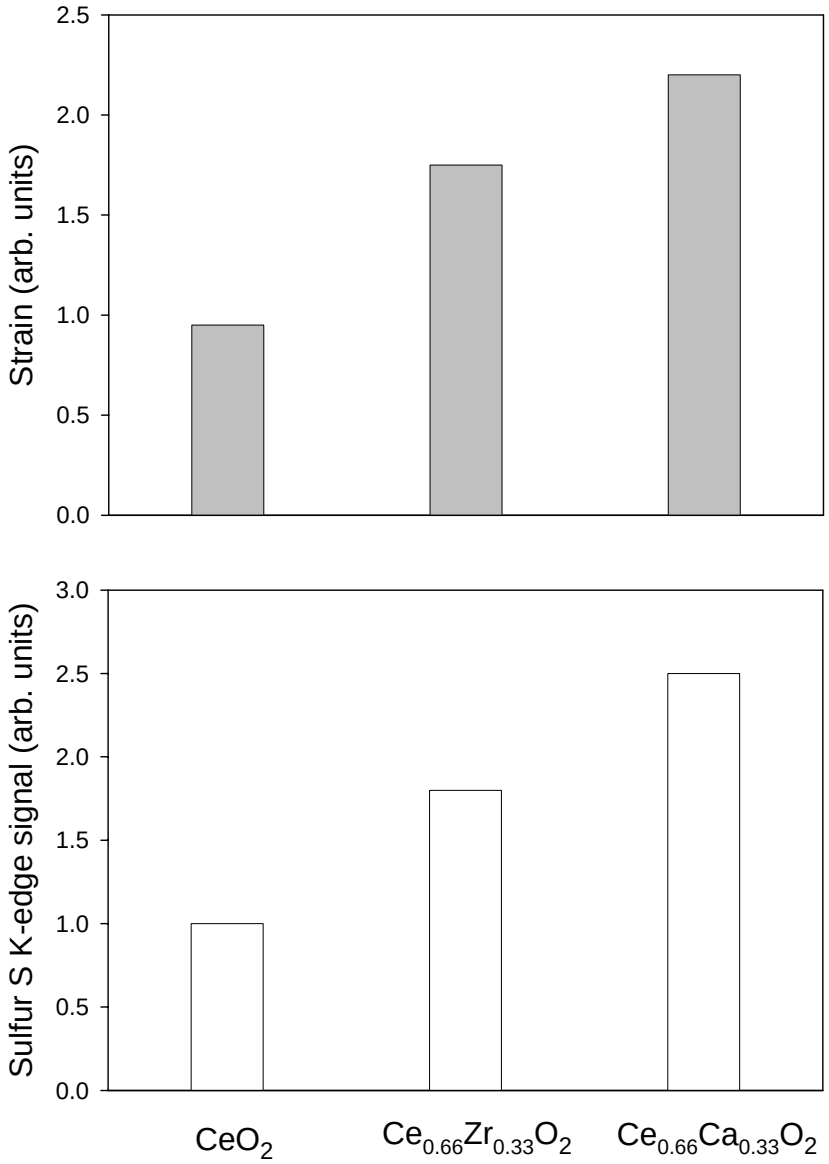
Strain (arb. units)
2.5
2.0
1.5
1.0
0.5
0.0
Sulfur S K-edge signal (arb. units)
3.0
2.5
2.0
1.5
1.0
0.5
0.0
CeO2
Ce0.66Zr0.33O2
Ce0.66Ca0.33O2

Fig. 8

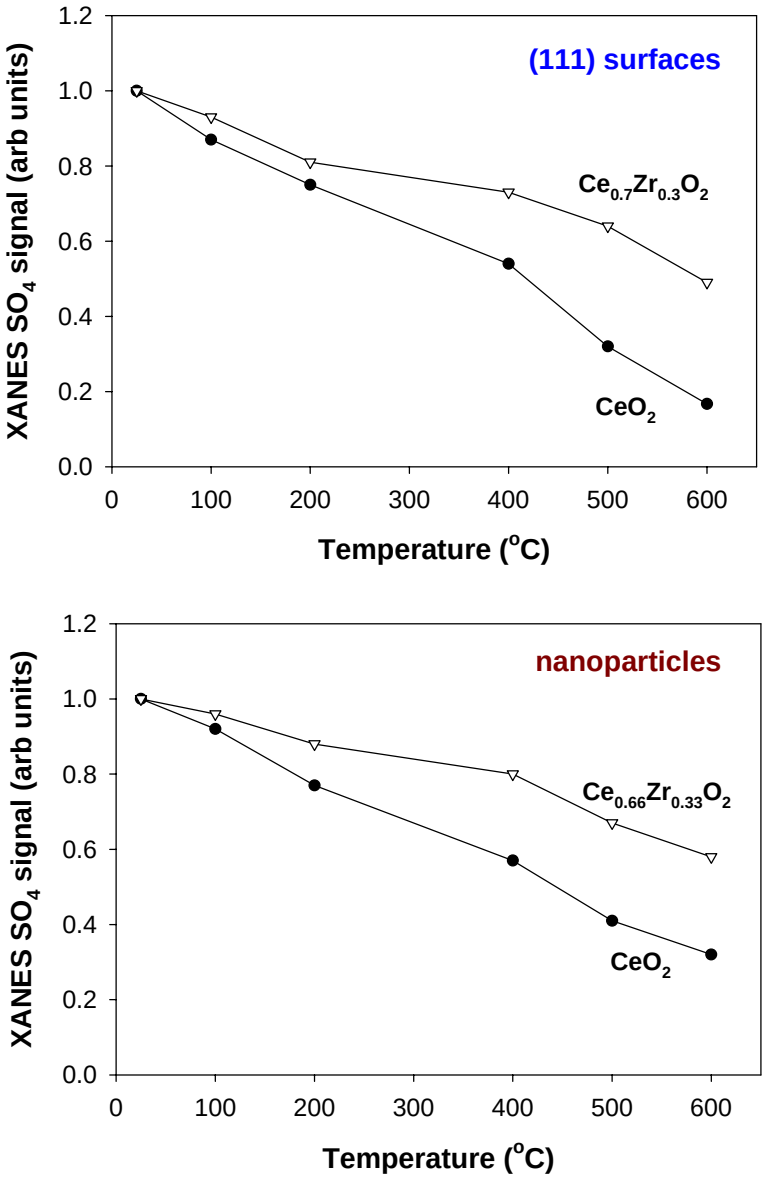
(111) surfaces
$Ce_{0.7}Zr_{0.3}O_2$
CeO_2
XANES SO_4 signal (arb units)
Temperature (^oC)
nanoparticles
$Ce_{0.66}Zr_{0.33}O_2$
CeO_2
XANES SO_4 signal (arb units)
Temperature (^oC)

Fig. 9